Supplementary Information For

Cerebellar granule cells acquire a widespread feedback control signal during motor learning

Andrea Giovannucci[1,2 †], Aleksandra Badura[1,3 †], Ben Deverett[1,4], Farzaneh Najafi[5,*] Talmo D. Pereira[1], Zhenyu Gao[6], Ilker Ozden[1,7], Alexander D. Kloth[1,**], Eftychios Pnevmatikakis[2,8], Liam Paninski[8], Chris I. De Zeeuw[3,6] Javier F. Medina[9], Samuel S.-H. Wang[1]

[1]Princeton Neuroscience Institute and Department of Molecular Biology, Princeton University, Princeton, NJ, USA. [2]Simons Center for Data Analysis, Simons Foundation, New York, NY, USA.[3]Netherlands Institute for Neuroscience, Amsterdam, The Netherlands. [4]Robert Wood Johnson Medical School, New Brunswick, NJ, USA. [5]Department of Biology, Univ. of Pennsylvania, Philadelphia, PA, USA. [6]Department of Neuroscience, Erasmus MC, Rotterdam, The Netherlands. [7]Department of Physics and Division of Engineering, Brown University, Providence, RI, USA. [8]Departments of Statistics and Neuroscience, Columbia University, New York, New York, USA. [9]Department of Neuroscience, Baylor College of Medicine, Houston, TX, USA.

* Current address: Cold Spring Harbor Laboratory, Cold Spring Harbor, NY, USA.
** Current address: University of North Carolina, Chapel Hill, NC, USA.
† Equal contributions.

Correspondence: Samuel S.-H. Wang
Princeton Neuroscience Institute, Washington Road
Princeton University
Princeton, NJ 08544
Tel: (609) 258-0388
Email: sswang@princeton.edu

Javier F. Medina
Department of Neuroscience
Baylor College of Medicine
One Baylor Plaza, Room S709
Houston, TX 77005
Tel: (713) 798-8141
Email: jfmedina@bcm.edu

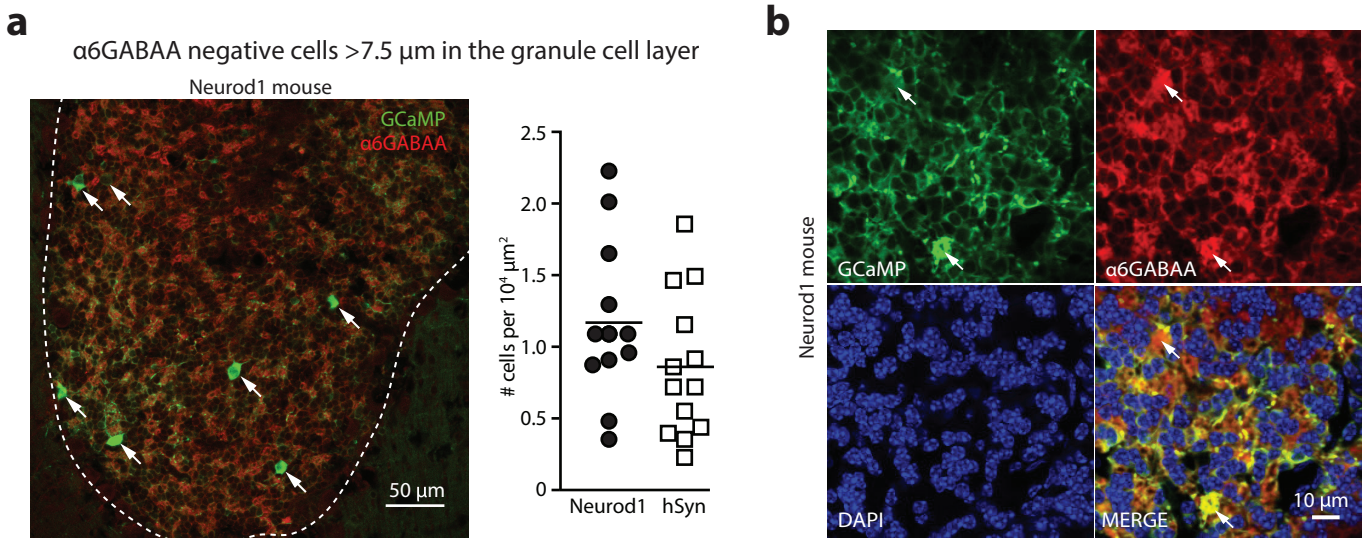

Figure ED 1. GCaMP-positive structures in the granule cell layer are predominantly granule cells. (**a**) A Neurod1 mouse injected with AAV1.CAG.Flex.GCaMP6f.WPRE.SV40. GCaMP6f (green) positive cells negative for α6GABAA (red) were sparse in the granule cell layer, and are indicated by white arrows. The dashed white line denotes the location of Purkinje cells at the border between granule and molecular layers. The scatter plot shows absolute numbers of α6GABAA negative cells >7.5 μm wide in the granule cell layer in 10,000 μm^2 fields of view. Horizontal bars represent means (Neurod1 = 1.2±0.6, and hSyn = 0.9±0.5). (**b**) High-magnification images of the granule cell layer revealed that the majority of round, small (between 4.5 and 7.5 μm in diameter) GCaMP6f-positive structures were both positive for α 6GABAA and contained a distinct nucleus revealed by DAPI staining. White arrows point to putative granule cell dendrites, positive for both GCaMP6f and α6GABAA but without nuclear staining.

Supplementary Movie ED2. Calcium signaling in GCaMP-expressing parallel-fiber boutons.

A B6.Cg-Tg(NeuroD1-Cre).GN135.Gsat mouse was injected with 200 nL of AAV1.CAG.Flex.GCaMP6f.WPRE.SV40. Spontaneous activity in parallel-fiber boutons of lobule VI was recorded in a mouse walking on a cylindrical treadmill. Images were acquired at 512 by 128 pixels (130x30 µm), 10 ms per frame. Playback speed, 20 Hz (5x slower than acquisition).

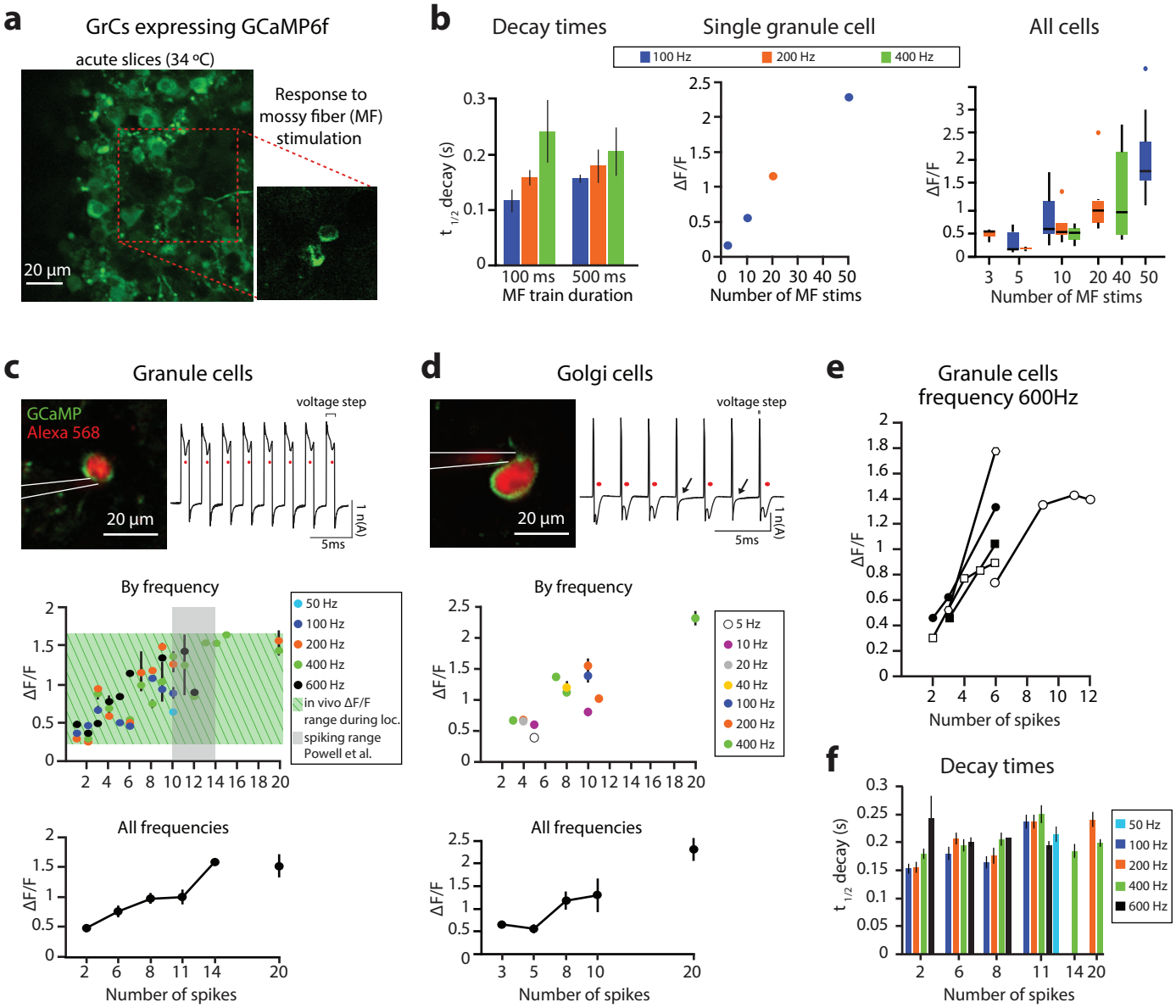

Figure ED3. GCaMP6f signals in cerebellar brain slices.
(a) Granule cells (GrCs) expressing GCaMP6f in a brain slice imaged under two-photon microscopy. The inset shows a fluorescence image of two GrCs during stimulation of mossy fibers via a saline-filled glass electrode placed more than 100 microns away. (**b**) Signal decay times and amplitudes in GrCs recorded using mossy fiber (MF) stimulation (n=8). The center subpanel represents data from a single GrC. (**c**) GCaMP signals evoked by direct depolarization of GrCs. *Top.* A GCaMP-expressing GrC counterstained with Alexa 568 electroporated into the cell by repeated depolarization and recorded by a cell-attached patch pipet. Action potentials (red dots) were evoked by applying voltage steps to the recording pipet of 200 mV, 1 ms. *Middle.* Fluorescence signals as a function of the number of evoked action potentials from all recorded cells (n=18); shaded areas indicate ΔF/F range *in vivo* during locomotion (green) and spiking range of GrCs recorded *in vivo* by Powell et al. (grey; Powell et al. eLife, 2015). *Bottom.* Averaged data (bin size 3 spikes). (**d**) Similar recordings for Golgi cells (n=2). (**e**) GCaMP signal amplitudes in five GrCs stimulated to fire 2-12 action potentials at 600 Hz by cell-attached pipet. (**f**) Decay times of depolarization-triggered firing.

Supplementary Movie ED4. Granule cell identification by constrained matrix factorization. **Raw Data**. Original movie after motion correction (horizontal black bands arise from motion correction). The red circles indicate four granule cells identified by the factorization procedure. **Denoised**. Data with noise removed and synchronized neuropil activity retained. **No Neuropil**. Denoised movie with neuropil contribution to each pixel removed. **Neuropil synchronized activity**. Activity of the neuropil displayed separately from neurons.

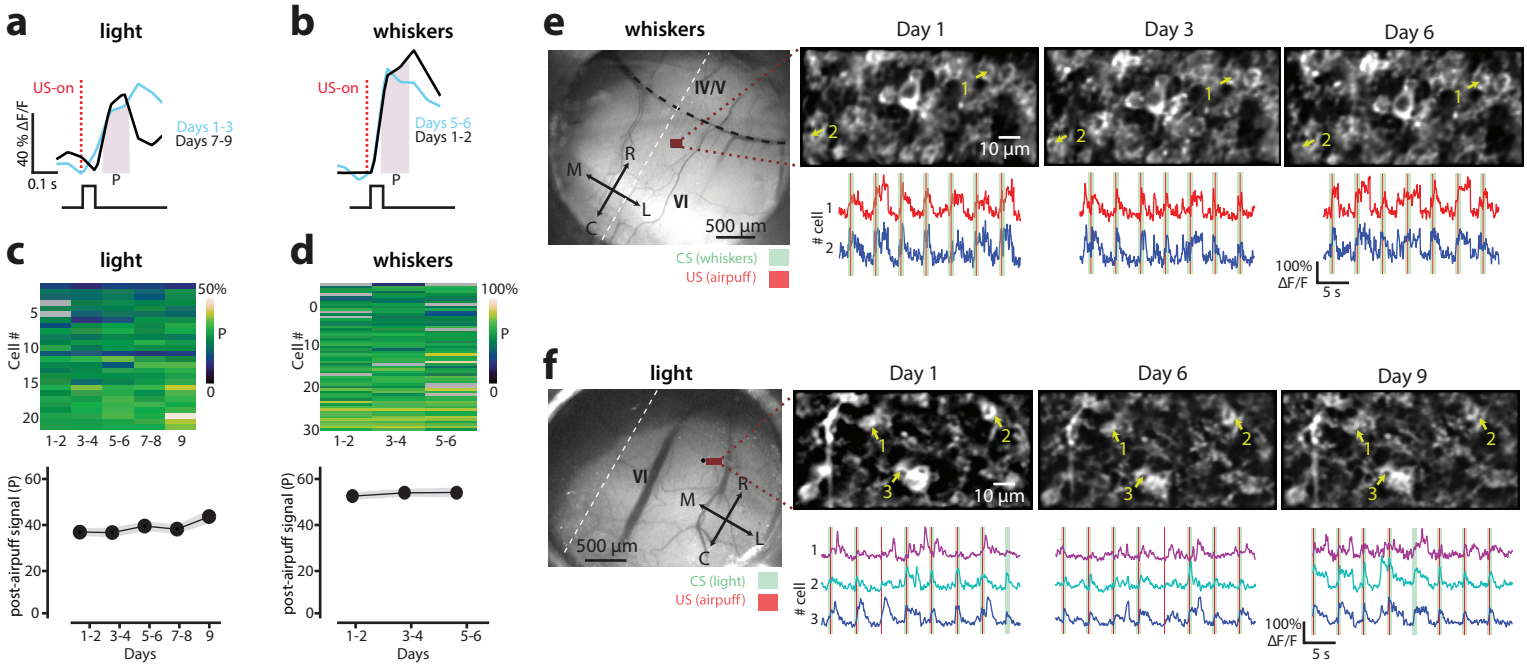

Figure ED 5. Stability of granule cell response properties across days.

(a) For light CS mouse, average calcium traces in response to periorbital airpuff stimulation on days 1-3 (blue) and 7-9 (black). (**b**) Same as (a), but for a whisker CS in days 1-2 (black) and 5-6 (blue). As a measure of granule cell responses to US stimulus, P was defined as the integral of the response between 64 and 240 msec after US stimulus delivery. (**c-d**) Evolution of the response to periorbital stimulation in individual granule cells during training for light (panel c) and whisker (panel d) CS animals. The response was stable across days, so the variation in CS responses observed during training did not arise from changes in neuronal physiology nor as an artifact of data analysis. (**e-f**) Two-photon imaging of granule cell activity. (**e**) Craniotomy over cerebellar lobule VI in example whisker-CS mouse. The dashed lines indicate the interlobule boundary (black) and the brain midline (white). In fields of view across training yellow arrows indicate representative cells. Corresponding granule cell fluorescence traces are shown underneath. Shaded areas indicate times of stimulus delivery. (**f**) Craniotomy over cerebellar lobule VI in example light-CS mouse. The dashed lines indicate the brain midline (white). In fields of view across training yellow arrows indicate representative cells. Corresponding granule cell fluorescence traces are shown underneath. Shaded areas indicate times of stimulus delivery.

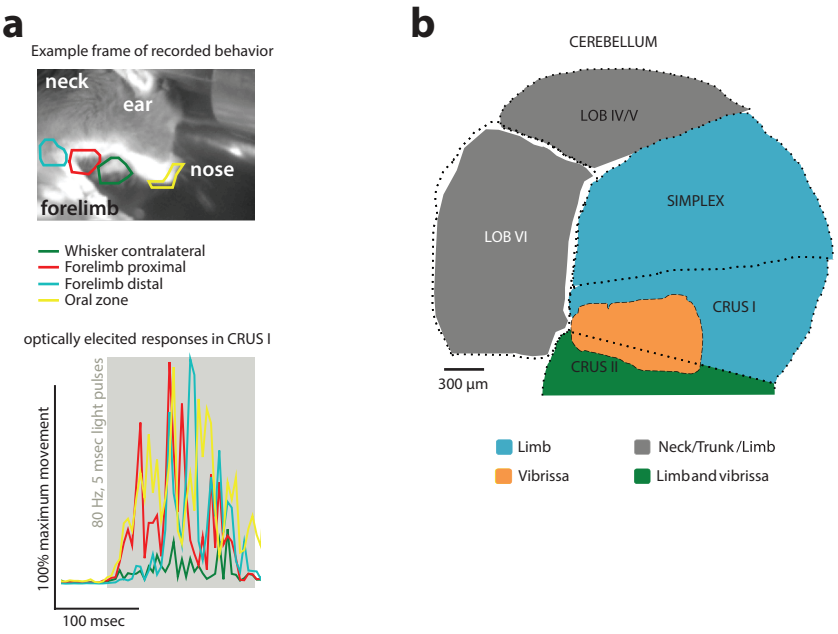

Figure ED 6. Channelrhodopsin-2 optogenetic stimulation of cerebellar mossy fibers.
(a) *Top*. Frame from camera recording behavior along with different zones marked for the animal: whiskers (green), forelimb proximal (red), forelimb distal (cyan) and oral zone (yellow). *Middle*. Corresponding regions of interest matching the colors in the top image. *Bottom*. Movements elicited by stimulation of Crus I surface. **(b)** Coarse map of responses elicited by cerebellar stimulation.

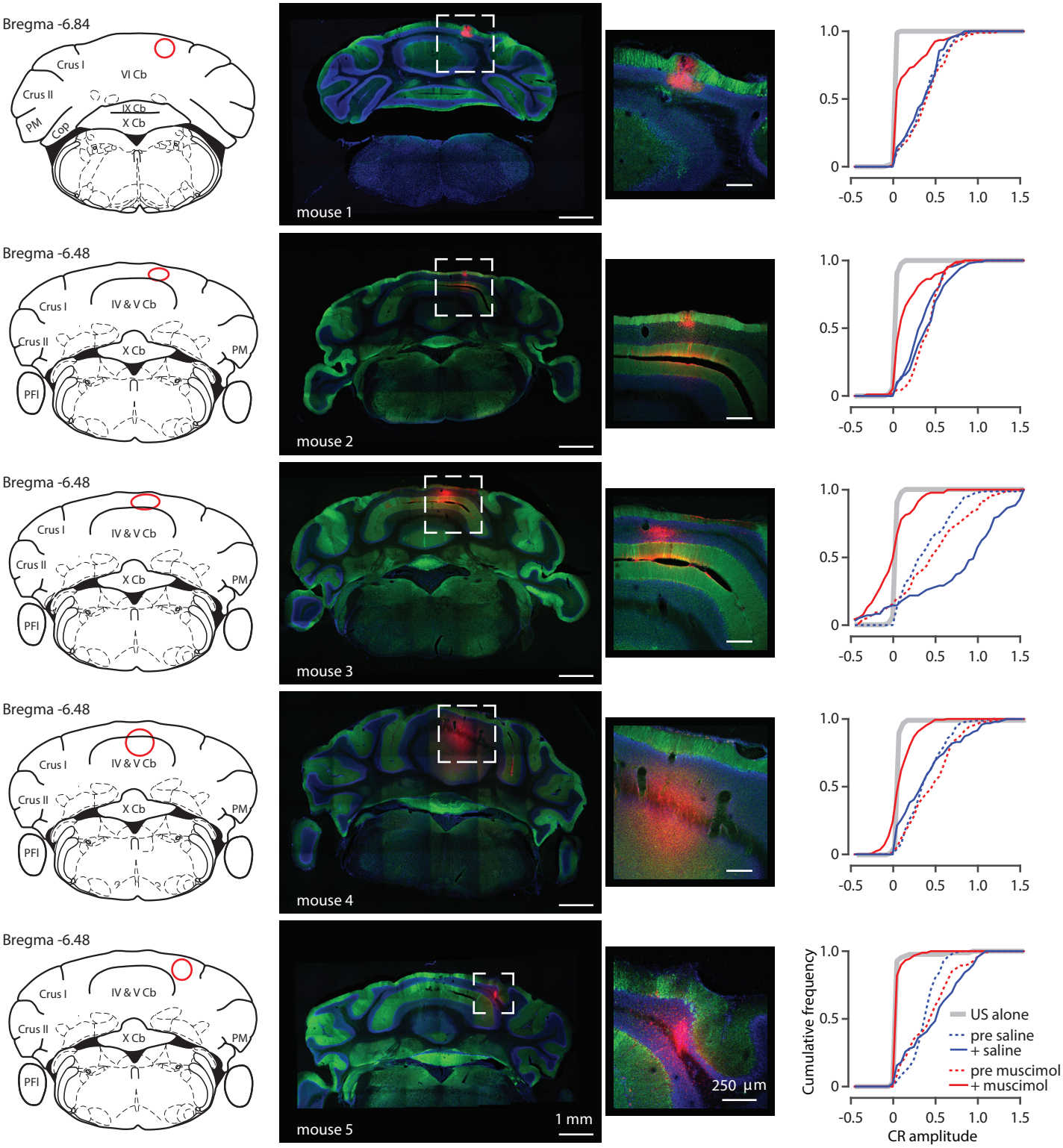

Figure ED7. Pharmacological inactivation in all tested animals.

Left column. Red circles depict size and location of the muscimol injections using the Allen Brain Atlas coordinate system in cerebellar coronal sections. Distance from bregma is indicated next to each section. *Middle column*. Cerebellar coronal sections from all mice used in the experiments. Location and extent of muscimol injections is shown in red. Muscimol was mixed with Evans Blue and visualized by excitation at 594 nm. Sections were counterstained with DAPI (blue) and aldolase C antibody to reveal zebrin-positive and zebrin-negative zones in the Purkinje cell layer (green). *Right column*. Cumulative frequency graphs of the amplitude of conditioned responses in trained animals during baseline before saline injection. Pre-saline, blue dashed line. After saline injections ("+ saline"), blue solid line. During baseline before muscimol injections, red dashed line. After muscimol, red solid line. US-only trials are plotted as a gray line for reference.

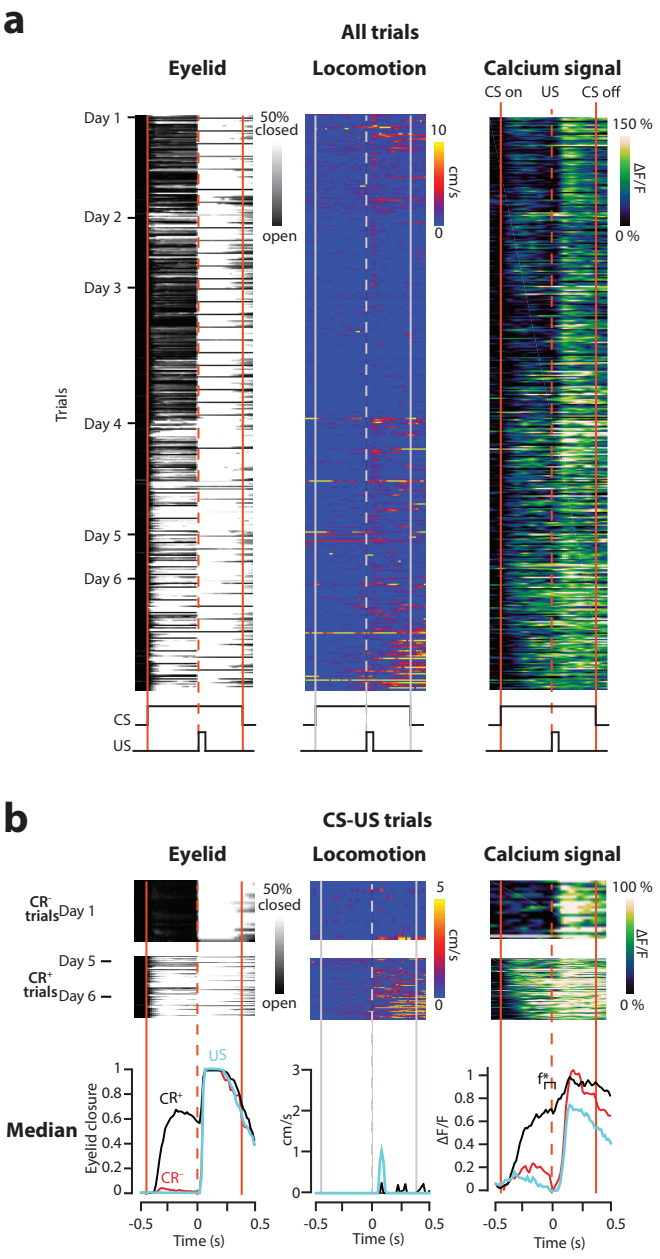

Figure ED8. Monitoring representations in cerebellar granule cells over the course of learning (whisker CS).

(**a**) Eyelid movement (left), wheel movement (middle), and neural activity in an example granule cell (right) over six days of CS-plus-US training. Each row represents a single trial. Minor ticks indicate a new session on the same day of training. Vertical solid lines indicate onset and offset of CS stimulus, dashed vertical lines indicate delivery time of the US stimulus. (**b**) In CS-US trials, data grouped according to whether the CS did ("CR+", middle) or did not ("CR–", top) evoke an anticipatory eyelid closure. Bottom. Overlaid average responses of the two conditions above plus US trials. f* is the integral of the neural response 260-440 msec after CS onset.

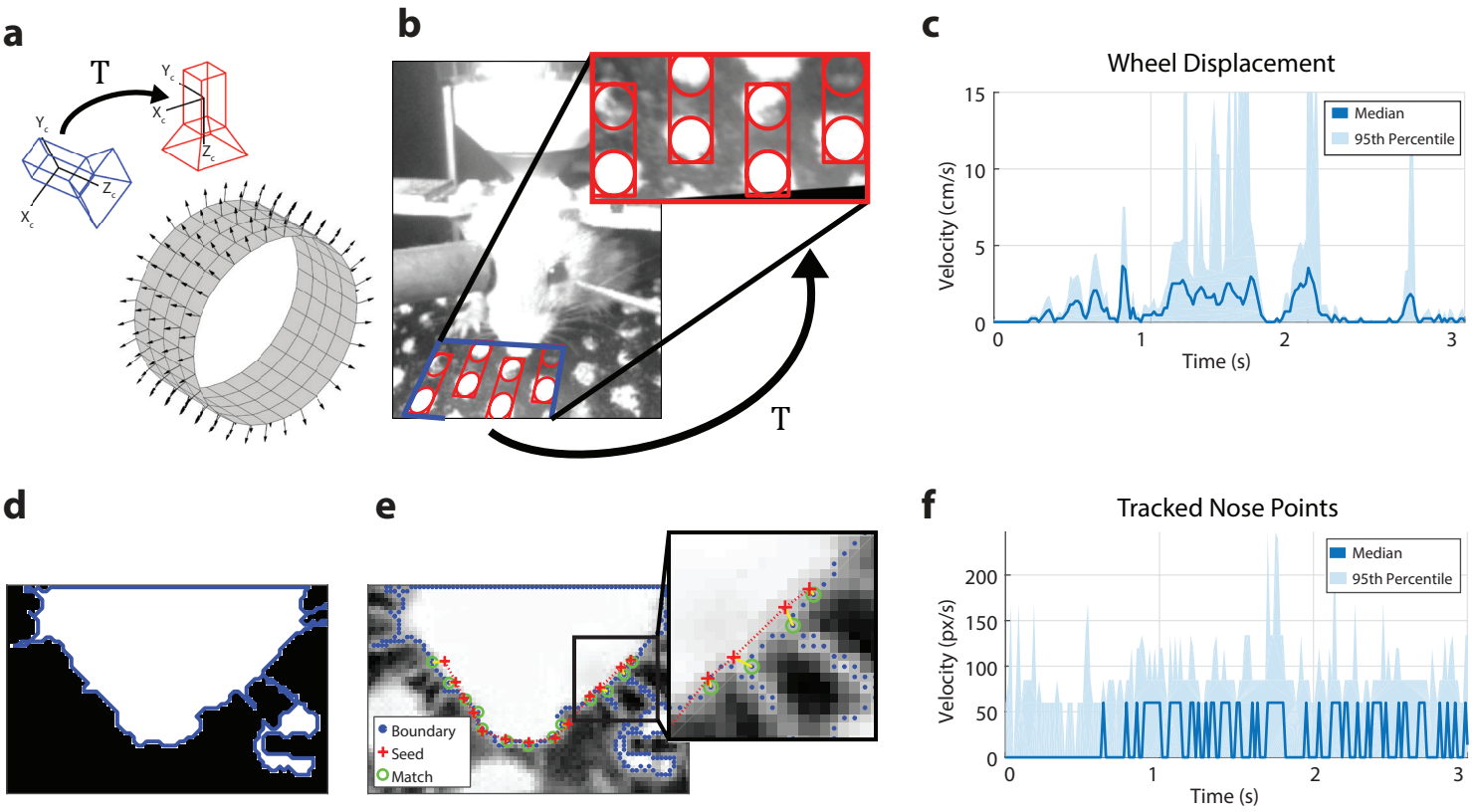

Figure ED9. Measures of animal motion were estimated from images of behavioral recordings. (**a**) Because the behavior camera (blue) was positioned non-orthogonally to the wheel's surface (black arrows), a model based on physical measurements of the wheel was used to estimate a projective transform (T) that reprojected image pixels onto the imaging plane of a theoretically orthogonally positioned camera (red). (**b**) By applying this transform to a region of the image containing mostly wheel pixels (blue), a reprojected view was computed (red) such that vertical displacements corresponded directly to wheel motion. (**c**) After tracking regions in the projected images, an estimate of the actual physical velocity could be calculated by scaling to the model parameters. To compensate for image noise, all pixels in the fictive field of view were tracked and their displacements yielded a distribution whose summary measures quantitatively reflected animal locomotion. (**d**) In order to measure animal self-motion, raw images were segmented and their boundaries traced to yield a set of points that putatively included the contour of the snout. (**e**) Seed points (red) were selected along the contour of the snout and then matched (green) to boundary points (blue) across subsequent frames via a robust point set registration algorithm. This approach was capable of dealing with substantial noise (inset) by imposing constraints on the rigidity of the original contour. (**f**) All seed points around the contour of the snout were tracked across time and their absolute displacements yielded a distribution over point velocities. Despite nonlinear shape deformations, summary measures of these point velocities served as a robust estimate for animal self-motion.

Supplementary Movie ED10. **Wheel tracking corrects for perspective and estimates locomotor velocity**. *Left*. A model of the wheel was constructed from physical measurements and manually fitted to the behavioral recording of the animal. *Top-right*. The parameters of the model defined a projective transform to remap the image pixels to the perspective of the surface normal of the wheel. *Bottom-right*. The tracked vertical displacement of the reprojected wheel pixels was rescaled to physical units to estimate the true instantaneous locomotor velocity.

Supplementary Movie ED11. **Snout motion is quantified by tracking snout shape trajectories**. *Left*. The outline of the shape of the snout was manually traced to provide a set of seed points that was displaced when the animal generated facial movements. *Top-right*. The images were thresholded and a robust point set registration algorithm was applied to track the trajectories of the seed points even when segmentation was made difficult by background artifacts. *Bottom-right*. The magnitude of the seed point velocities was used as a measure of facial movements.

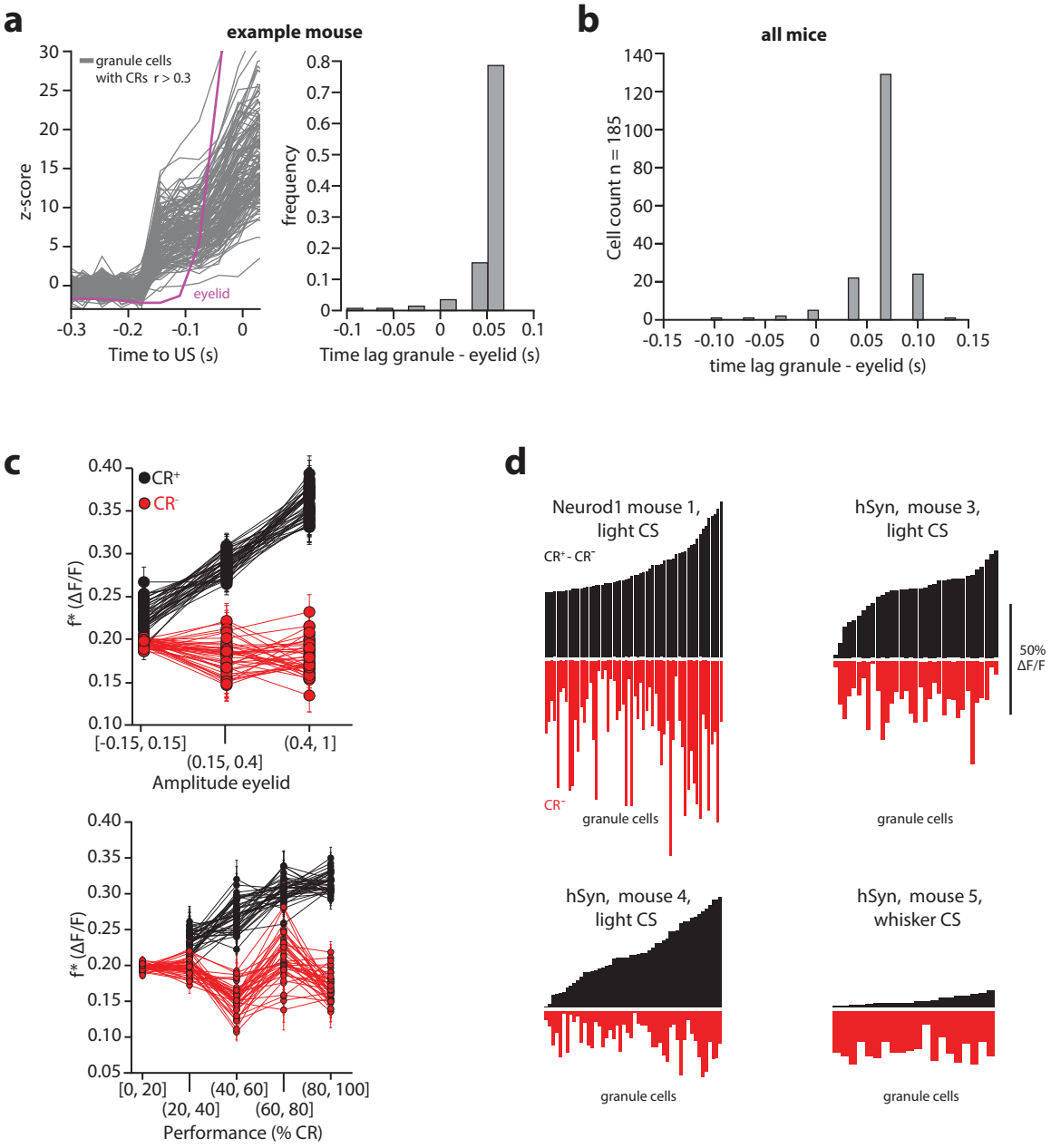

Figure ED 12. Response properties of granule cells.
(**a**) *Left*. Example of traces that are highly correlated with CR (r for CR>0.3) superimposed on averaged eyelid response during the CR^+ trials in the last training session in 1 mouse. Traces are normalized to the standard deviation of the noise computed over the pre stimulus period. *Right*. Histograms of latencies corresponding to the traces on the left. Latencies were calculated between the onset of the average conditioned response in CR^+ trials (first crossing of the 3 standard deviation threshold) and the onsets of each neuron averaged in CR^+ trials (same normalization and 3 standard deviation crossing). Data comes from a mouse scanned using a fast resonant scanner. (**b**) Histograms of latencies as described in (a) calculated for all granule cell responses strongly correlated with the CR (r>0.3) in all mice. (**c**) 40 runs of the bootstrapping procedure sampling f* in CR^+ (black) and CR^- (red) trials from 30 neurons per FOV per animal (N=6) and then binned according to eyelid amplitude (top) or performance (% CR, bottom). (**d**) Histograms of granule cell responses in 4 fully trained mice. Each histogram bar represents the response of a single granule cell to a CS stimulus without wheel movement. Red histograms show ΔF/F for trials with no conditioned response (CR^-, same time bin as f*). Black histograms show difference in ΔF/F between CR+ and CR^- trial responses for the same cells, i.e. the CR+ excess (same time bin as f*). One field of view from each mouse.